









Engineering the Cu/Mo₂CT_x (MXene) interface to drive CO₂ hydrogenation to methanol

Journal Article

Author(s):

Zhou, Hui; [Chen, Zixuan](#) ; Vidal López, Anna; Díaz López, Estefanía; Lam, Erwin; Tsoukalou, Athanasia; Willinger, Elena; [Kuznetsov, Denis](#) ; Mance, Deni; [Kierzkowska-Stürzlinger, Agnieszka](#) ; [Donat, Felix](#) ; [Abdala, Paula Macarena](#) ; [Comas Vives, Aleix](#) ; [Copéret, Christophe](#) ; [Fedorov, Alexey](#) ; Müller, Christoph R.

Publication date:

2021-10

Permanent link:

<https://doi.org/10.3929/ethz-b-000512844>

Rights / license:

[Creative Commons Attribution 4.0 International](#)

Originally published in:

Nature Catalysis 4(10), <https://doi.org/10.1038/s41929-021-00684-0>

Funding acknowledgement:

800419 - Sorbent-enhanced Steam Biomass Reforming for Integrated Bio-energy with Carbon Capture and (EC)

819573 - Advancing CO₂ Capture Materials by Atomic Scale Design: the Quest for Understanding (EC)

ETH-40 17-2 - Advanced materials by atomic layer deposition (ALD): from controlling porosity of ALD-grown overcoats to the molecular understanding of silica-aluminas (ETHZ)

ETH-44 16-2 - The direct integration of CO₂ conversion into CO₂ capture: Development of model bi-functional Cu-MgO-MO_x materials through the elucidation of the carbonation mechanism and active sites for CO₂ hydrogenation (ETHZ)

Engineering the Cu/Mo₂CT_x (MXene) Interface to Drive CO₂ Hydrogenation to Methanol

Hui Zhou,¹ Zixuan Chen,¹ Anna Vidal López,² Estefanía Díaz López,² Erwin Lam,³ Athanasia Tsoukalou,¹ Elena Willinger,¹ Denis A. Kuznetsov,¹ Deni Mance,³ Agnieszka Kierzkowska,¹ Felix Donat,¹ Paula M. Abdala,¹ Aleix Comas-Vives,^{2*} Christophe Copéret,^{3*} Alexey Fedorov,^{1*} and Christoph R. Müller^{1*}

*Corresponding author. Email: Aleix.Comas@uab.cat; ccoperet@ethz.ch; fedoroal@ethz.ch; muelchri@ethz.ch

Affiliations ¹Department of Mechanical and Process Engineering, ETH Zürich, CH-8092 Zürich, Switzerland. ²Department of Chemistry, Autonomous University of Barcelona, 08193 Cerdanyola del Valles, Catalonia, Spain. ³Department of Chemistry and Applied Biosciences, ETH Zürich, CH-8093 Zürich, Switzerland.

Abstract

Development of efficient catalysts for the direct hydrogenation of CO₂ to methanol is essential for the valorization of this abundant feedstock. Here we show that a silica-supported Cu/Mo₂CT_x (MXene) catalyst achieves a higher intrinsic methanol formation rate per mass Cu than the reference Cu/SiO₂ catalyst with a similar Cu loading. The Cu/Mo₂CT_x interface can be engineered owing to the higher affinity of metallic Cu for the partially reduced MXene surface (in preference to the SiO₂ surface) and the mobility of Cu under H₂ at 500 °C.

Increasing the reduction time, the Cu/Mo₂CT_x interface becomes more Lewis acidic due to the higher amount of Cu⁺ sites dispersed onto the reduced Mo₂CT_x and this correlates with an

increased rate of CO₂ hydrogenation to methanol. The critical role of the interface between Cu and Mo₂CT_x is further highlighted by DFT calculations that identify formate and methoxy species as stable reaction intermediates.

Introduction

Carbon dioxide, a major contributor to climate change, is potentially an abundant carbon resource for chemicals and fuels. Among the different approaches for CO₂ conversion, the direct catalytic hydrogenation of CO₂ to methanol is an emerging technology for decreasing CO₂ emissions and storing renewable hydrogen obtained from intermittent solar or wind energy, forming thereby the basis of the methanol economy^{1,2}. While the industrial Cu-based methanol synthesis catalyst, Cu-ZnO-Al₂O₃^{3,4}, is efficient in converting a mixture of H₂, CO and CO₂ (i.e. synthesis gas) to methanol, this catalyst has generally been considered to be less efficient with CO₂-rich feeds, especially at lower space velocities,^{3,5-10} although there is some counter evidence¹¹. By using specific supports, e.g. Cu/ZrO₂¹²⁻¹⁴, the catalytic performance of Cu-based catalysts for the direct CO₂ hydrogenation to methanol can be improved; however, the activity and selectivity of these catalysts are currently insufficient for their industrial deployment. A complementary counterexample is Cu on reducible supports such as TiO₂ or CeO₂, that mostly leads to the formation of CO via the reverse water-gas shift reaction (RWGS) resulting in low production rates of methanol¹⁴⁻¹⁶. Overall, the nature of the support and the Cu-support interface are essential parameters for controlling the catalyst performance¹⁷⁻¹⁹. For instance, the introduction of isolated Ti(IV) and Zr(IV) surface sites to Cu/SiO₂, which itself is a poor methanol synthesis catalyst, significantly improves its activity and selectivity, making it on par with Cu/ZrO₂^{13,15}.

In contrast to reducible oxides that are prone to strong metal-support interaction (SMSI), leading to the overcoating of metal particles with a reduced support, i.e. a geometric effect),

transition-metal carbides feature electronic metal-support interactions^{20–24}. MXene materials, i.e. a family of two-dimensional (2D) carbides, nitrides, and carbonitrides^{25–27} with the general formula of $M_{n+1}X_nT_x$ (where M is an early transition metal, $n = 1, 2, 3$, X is C and/or N, and T are surface $-O-$, $-OH$, and/or $-F$ groups), are currently emerging in thermocatalytic applications as catalysts^{28–30} or supports with reactive metal-support interactions^{31–34}. MXenes without surface termination groups are oxophilic and therefore bind and activate CO_2 strongly³⁵.

Here we report that silica-supported, dispersed, reducible nanosheets of a delaminated molybdenum MXene, Mo_2CT_x , can be used to engineer a Cu/Mo_2CT_x interface that shows a ca. six times increased copper-normalized intrinsic formation rate of methanol by the direct hydrogenation of CO_2 as compared to Cu/SiO_2 , and a higher selectivity to methanol at higher CO_2 conversions (ca. 37% at $X(CO_2) = 3.2\%$ under 25 bar). To develop this silica-supported catalyst ($Cu/Mo_2CT_x/SiO_2$), we rely on surface organometallic chemistry (SOMC),³⁶ to graft a copper mesityl precursor onto Mo_2CT_x/SiO_2 . Treatment of the grafted material in H_2 leads to the migration of Cu from the silica surface onto the Mo_2CT_x nanosheets. *Operando* diffuse reflectance infrared Fourier transform spectroscopy (DRIFTS) and solid-state nuclear magnetic resonance (ssNMR) using ^{13}C -labelled CO_2 and H_2 indicate the presence of surface formate and methoxy intermediates at the Cu/Mo_2CT_x interface in higher abundance as compared to the reference Cu/SiO_2 interface, correlating directly with the higher catalytic activity of $Cu/Mo_2CT_x/SiO_2$, which is further confirmed by density functional theory (DFT) calculations. Finally, Cu L_3VV Auger spectra and DRIFTS data using CO as a probe molecule indicate that the increased catalytic activity of $Cu/Mo_2CT_x/SiO_2$ is associated with a higher fraction of Lewis acidic Cu^+ sites at the Cu/Mo_2CT_x interface, which is supported by DFT calculations.

Results

Synthesis and characterization of Cu/Mo₂CT_x/SiO₂

Delaminated atomically thin nanosheets of Mo₂CT_x were dispersed from a colloidal solution (Supplementary Figure 1) onto a silica support, using incipient wetness impregnation according to a previously reported method developed in our group³⁰. The resulting Mo₂CT_x/SiO₂ material (0.3 wt% Mo loading, Fig. 1a and Supplementary Figure 2) was then dehydroxylated at 500 °C under N₂ flow, yielding Mo₂CT_x/SiO₂₋₅₀₀ with 0.47 mmol g⁻¹ of ≡SiOH sites according to titration with dibenzyl magnesium. The dehydroxylation of the silica surface does not affect the integrity of the supported Mo₂CT_x nanosheets, at least up to 800 °C as previously reported³⁰. We then grafted [Cu_n(Mesityl)_n, n = 2, 4, 5, (CuMes)] onto Mo₂CT_x/SiO₂₋₅₀₀ in toluene using 0.83 equiv. of Cu per silanol site. The infrared (IR) spectrum of the grafted material shows the consumption of the isolated ≡SiOH band at 3745 cm⁻¹ and the appearance of new C–H bands at 3019, 2925, 2868, and 1597 cm⁻¹ (Fig. 1b), indicating the successful grafting of CuMes on ≡SiOH sites^{15,37}. Treatment under H₂ at 500 °C for 2 h restored the ≡SiOH groups while C–H stretching bands disappeared (Fig. 1b) due to the complete hydrogenolysis of the grafted CuMes precursor in this material, denoted Cu/Mo₂CT_x/SiO_{2-2h} (the time of the H₂ treatment is indicated in the subscript notation). Increasing the time of the H₂ reduction to 6 h gave the Cu/Mo₂CT_x/SiO_{2-6h} material. We also prepared silica-supported Cu nanoparticles via the same approach using CuMes as a precursor (i.e. reference Cu/SiO_{2-2h} catalyst), as previously reported^{17,36,37}. In what follows, we contrast the nature of the Cu/support interface with the performance of Cu/SiO_{2-2h}, Cu/Mo₂CT_x/SiO_{2-2h}, Cu/Mo₂CT_x/SiO_{2-6h} as well as the industrial Cu-ZnO-Al₂O₃ benchmark for the hydrogenation of CO₂ to methanol.

High-angle annular dark-field scanning transmission electron microscopy imaging (HAADF-STEM) shows small Cu nanoparticles (NPs) with a narrow size distribution (2.9 ± 0.4 nm) on the SiO₂ surface, for both Cu/Mo₂CT_x/SiO₂ materials and for the Cu/SiO_{2-2h} reference material (unless specified otherwise, specimens were exposed to ambient air prior to analysis with transmission electron microscopy (TEM), Supplementary Figure 3). The Cu loadings, as determined by inductively coupled plasma (ICP) analysis, are similar in the catalysts, i.e. 2.4 and 2.0 wt% Cu for Cu/Mo₂CT_x/SiO_{2-2h} and Cu/SiO_{2-2h}, respectively. Energy-dispersive X-ray spectroscopy (EDX) of two distinct areas in Cu/Mo₂CT_x/SiO_{2-2h} confirms that Cu is dispersed on both SiO₂ and Mo₂CT_x (Regions 1 and 2, respectively, in Fig. 1c). Interestingly, the intensity of the Cu signal (normalized by the Si signal) on Mo₂CT_x (Region 2) is 3.2 times higher than that on SiO₂ (Region 1), indicating that Cu is enriched on the Mo₂CT_x phase in preference to SiO₂. Performing a similar analysis of the intensities of the Cu signal in CuMes/Mo₂CT_x/SiO₂ (i.e. the material prior to H₂ reduction) shows that Cu is dispersed uniformly on Mo₂CT_x and SiO₂ (Supplementary Figure 4). These results indicate the mobility of Cu during the H₂ treatment at 500 °C and the preferential migration of Cu from SiO₂ onto Mo₂CT_x.

We also characterized Cu/Mo₂CT_x/SiO_{2-2h} by high-resolution HAADF-STEM without exposing this material to air (Fig. 1d–f). Mo₂CT_x nanosheets are found to cover approximately one third of the silica surface. Stacking faults of the Mo₂CT_x lattice can be observed, indicated by the fast Fourier transform (FFT) pattern (Fig. 1d), which suggests the presence of Mo vacancies in Mo₂CT_x that may serve as interaction sites for Cu atoms^{34,38}. Interestingly, while the SiO₂ surface that is not covered by MXene nanosheets in Cu/Mo₂CT_x/SiO_{2-2h} contains Cu nanoparticles of ca. 3 nm in diameter, the Cu on the Mo₂CT_x nanosheets has a higher dispersion, including few-atoms-small clusters and single Cu atoms (circles, Fig. 1e). It is worth noting that the edges of the Mo₂CT_x nanosheets are decorated

with, most probably, Cu atoms, as indicated by arrows in Fig. 1f, which is reminiscent of the coordination of transition metals to the edges of MoS₂ layers in hydrotreating catalysts³⁹ or the decoration of graphene edges by Cu atoms⁴⁰. This notable difference in the Cu speciation between the SiO₂ surface and Mo₂CT_x nanosheets is consistent with the high dispersion of Cu on β-Mo₂C that has been reported previously²³. No diffraction peaks due to Cu or Mo₂CT_x are observed in the X-ray powder diffraction (XRD) pattern of Cu/Mo₂CT_x/SiO_{2-2h} that shows mainly the diffuse scattering of the amorphous SiO₂ support (Supplementary Figure 5).

The amounts of surface Cu⁰ sites determined by N₂O titration⁴¹ (denoted Cu⁰(surf)) are 184.1, 78.4, and 59.4 μmol g_{cat}⁻¹ in Cu/SiO_{2-2h}, Cu/Mo₂CT_x/SiO_{2-2h}, and Cu/Mo₂CT_x/SiO_{2-6h}, respectively (Supplementary Table 1). The surface Cu⁰ sites account for 39% of the total Cu (measured by ICP analysis) in Cu/SiO_{2-2h} (Supplementary Table 1). In contrast, surface Cu⁰ sites contribute to only 21 and 16% of the total Cu sites in Cu/Mo₂CT_x/SiO_{2-2h} and Cu/Mo₂CT_x/SiO_{2-6h}, although similar particle size distributions are observed by TEM for Cu on the silica surface in Cu/SiO_{2-2h} and Cu/Mo₂CT_x/SiO₂. Note also that, as was discussed above, the Cu dispersion on the Mo₂CT_x nanosheets is notably higher than on the silica surface (small clusters and isolated atoms, Fig. 1d–f). Therefore, the lower fraction of surface Cu⁰ sites determined in Cu/Mo₂CT_x/SiO₂ compared to Cu/SiO_{2-2h} suggest the presence of surface Cu⁺ sites in these materials that do not react with N₂O (vide infra).

Catalytic performance of Cu/Mo₂CT_x/SiO₂

We then evaluated Cu/Mo₂CT_x/SiO_{2-6h}, Cu/Mo₂CT_x/SiO_{2-2h} and Cu/SiO_{2-2h} for the hydrogenation of CO₂ at 230 °C and 25 bar (H₂/CO₂/N₂ = 3/1/1). Compared to the reference catalyst Cu/SiO_{2-2h} (also prepared by SOMC), the intrinsic methanol formation rate of Cu/Mo₂CT_x/SiO_{2-2h} is over three times higher (1.51 vs. 0.41 g h⁻¹ g_{Cu}⁻¹, Fig. 1g), while the methanol selectivity is moderately higher (54% and 45%, Fig. 1g). Note that Mo₂CT_x/SiO_{2-2h}

(i.e. the respective material without Cu) exhibits only a low methanol space-time yield (STY) and 63% selectivity to CO via RWGS (Supplementary Figures 8 and 9). Using Cu/Mo₂CT_x/SiO_{2-6h}, which was prepared by increasing the duration of the treatment under H₂ to 6 h, leads to a further increase in the intrinsic methanol formation rate by 65% (to 2.49 g h⁻¹ g_{Cu}⁻¹ in Cu/Mo₂CT_x/SiO_{2-6h}) with a similar methanol selectivity of 52%. Contrary to the Cu/β-Mo₂C catalyst, no competing methanation of CO₂ was detected with Cu/Mo₂CT_x/SiO₂ catalysts, which contributes to a higher methanol selectivity on Cu/Mo₂CT_x/SiO₂ catalysts relative to Cu/β-Mo₂C²⁴. In addition, the Cu/Mo₂CT_x/SiO₂ catalysts developed in this study were compared to the benchmark Cu-ZnO-Al₂O₃ catalyst. We note that the amounts of active sites in Cu-ZnO-Al₂O₃ and Cu/Mo₂CT_x/SiO₂ catalysts are unknown. Therefore, we compare the intrinsic methanol formation rates in these catalysts after their normalization per Cu weight content (Fig. 1g and Supplementary Figures 10–12). Cu/Mo₂CT_x/SiO_{2-6h} exceeds the activity of the benchmark Cu-ZnO-Al₂O₃ catalyst (with high Cu loading) by 3.6 times (see Fig. 1g, Supplementary Figures 10–15, and Supplementary Table 3 for details). We note that the conversion of CO₂ is lower in experiments using the Cu/Mo₂CT_x/SiO₂ catalysts relative to the industrial Cu-ZnO-Al₂O₃ catalyst due to the higher loading of Cu in Cu-ZnO-Al₂O₃ catalyst, i.e. ca. 2.4 vs. 60 wt% Cu, respectively). At the same CO₂ conversion of 1.0%, the methanol selectivity increases as follows: Cu/SiO_{2-2h} < Cu/Mo₂CT_x/SiO_{2-2h} < Cu/Mo₂CT_x/SiO_{2-6h} (33, 42, and 47%, respectively, Fig. 1h). A comparison between the Cu/Mo₂CT_x/SiO₂ catalysts reduced at 350 or 500 °C for 6 h indicates that reduction at 500 °C provides a more active catalyst (Supplementary Figure 16). No further notable increase of the activity of Cu/Mo₂CT_x/SiO₂ is observed when extending the duration of the treatment under H₂ at 500 °C even further (i.e. > 6 h, Fig. 1i). A control experiment shows that when Cu/Mo₂CT_x/SiO₂ was pretreated in H₂ at 500 °C for 2 h first, followed by an additional 2 h pretreatment in N₂ at 500 °C, the activity did not increase, suggesting that H₂ is critical for

the activation of the catalyst. A similar influence of a longer H₂ pretreatment time on the activity of Cu/SiO₂ is not observed, indicating that the increase in activity was due to the interaction of Cu and Mo₂CT_x. These results imply that the Cu-Mo₂CT_x interaction (vide infra for the discussion of the nature of this interaction) and the high dispersion of Cu on Mo₂CT_x is critical to obtain an enhanced activity for CO₂ hydrogenation to methanol.

After more than 20 h of time on stream (TOS), the activity and selectivity of both Cu/Mo₂CT_x/SiO₂ catalysts remained unchanged, demonstrating a high stability of the material (Supplementary Figure 17). An experiment with more than 100 h TOS using Cu/Mo₂CT_x/SiO_{2-6h} was also performed and showed a stable methanol space time yield throughout the entire experiment, i.e. indicating no deactivation with TOS (Supplementary Figure 18). According to HAADF-EDX mapping (Supplementary Figure 19), the MXene morphology is preserved after 24 h of TOS of CO₂ hydrogenation, and the Cu distribution in the used Cu/Mo₂CT_x/SiO_{2-2h} catalyst is similar to that in the fresh material. No sintering of the Cu NPs on the SiO₂ surface (3.0 ± 0.3 nm) is observed (Supplementary Figure 3).

To understand how the Cu-Mo₂CT_x interface in the Cu/Mo₂CT_x/SiO₂ catalysts may influence the mechanistic pathways for CO₂ hydrogenation, we performed a contact time study by changing the flow rates of the reactants. While the intrinsic methanol formation rate is high for the Cu/Mo₂CT_x/SiO₂ catalysts, it decreases with increasing contact time and CO₂ conversion, i.e. for Cu/Mo₂CT_x/SiO_{2-6h} from 2.1 to 1.2 g h⁻¹ g_{Cu}⁻¹ at 0.7% and 3.2% CO₂ conversion, respectively (Supplementary Figure 6). However, the rates of Cu/Mo₂CT_x/SiO_{2-6h} are still 2.5 times higher than for the Cu/SiO_{2-2h} reference catalyst at the same contact time, which can be attributed to highly dispersed Cu on Mo₂CT_x nanosheets in Cu/Mo₂CT_x/SiO₂. A similar decrease in the methanol formation rate has been observed for other Cu-based catalysts and is explained by the inhibition of methanol formation pathways by reaction

products, i.e. water and/or methanol^{12,13}. In contrast, the CO formation rate increases slightly at long contact times for the Cu/Mo₂CT_x/SiO₂ catalysts. This result indicates that on Cu/Mo₂CT_x/SiO₂, the mechanisms leading to the products methanol and CO are different. In addition, the methanol formation rate does not change significantly with contact time for Cu/SiO_{2-2h}, implying different active sites in these two catalysts.

Rationale for higher activity of Cu/Mo₂CT_x/SiO_{2-6h}

One possible reason for the increasing activity of Cu/Mo₂CT_x/SiO₂ catalysts with increasing duration of the hydrogen treatment can be a different coverage of the Mo surface by T_x groups in the supported MXene nanosheets. We have shown previously that the oxygen surface coverage in 2D-Mo₂CO_x/SiO₂ influences drastically the catalytic properties of this catalyst in the dry reforming of methane³⁰. Therefore, we turned to X-ray photoelectron spectroscopy (XPS) analysis and fitted Mo⁵⁺, Mo⁴⁺, and carbidic Mo states in the Mo 3d XPS spectra of the MXene-derived materials (Supplementary Figure 20 and Supplementary Table 4). Mo is found mainly in the Mo⁵⁺ and Mo⁴⁺ states (69 and 22% fitted fractions, respectively) in CuMes/Mo₂CT_x/SiO₂ (i.e. before the H₂ treatment), due to the presence of abundant –O–, –OH, and –F groups oxidizing the surface after the synthesis of Mo₂CT_x (etching of the precursor phase Mo₂Ga₂C with 48% HF at 55 °C)⁴². XPS data shows no F 1s signal (688 eV) in Cu/Mo₂CT_x/SiO_{2-2h}, in contrast to CuMes/Mo₂CT_x/SiO₂ (Supplementary Figure 21). After the H₂ treatment at 500 °C (2 h), the fraction of carbidic Mo increases from 9 to 54% at the expense of Mo⁵⁺ and Mo⁴⁺ states that decrease to 41% and 5%, respectively. A further reduction of Mo is observed in Cu/Mo₂CT_x/SiO_{2-6h} (H₂ treatment at 500 °C for 6 h) as the fraction of Mo⁵⁺ in this material is 30%, while the Mo⁴⁺ state and carbidic Mo constitute 16% and 54%, respectively. After 24 h of TOS, the distribution of Mo states does not change notably, implying that surface Mo is not oxidized or reduced under CO₂ hydrogenation conditions (Supplementary Figure 22 and Supplementary Table 4).

Likewise, a continuous shift of Mo K-edge to lower energies was observed in an in situ X-ray absorption near edge structure (XANES) experiment, in which Cu/Mo₂CT_x/SiO_{2-0.5h}, exposed to ambient air during the transfer of the material to a capillary cell reactor, was heated from room temperature to 500 °C in a flow of H₂ (Supplementary Figure 23). During this temperature-programmed reduction (TPR) experiment, the average oxidation state of Mo, estimated from the Mo K-edge position of XANES spectra⁴³, reduced from ca. +4.4 in Cu/Mo₂CT_x/SiO_{2-0.5h} at room temperature (RT) in air, to ca. +0.9 after 6 h under H₂ flow (500 °C), i.e. close to the Mo oxidation state in β-Mo₂C²⁸. The ex situ Mo K-edge XANES spectra of CuMes/Mo₂CT_x/SiO₂ and Cu/Mo₂CT_x/SiO_{2-6h} (reduced in a laboratory reactor and handled without exposure to air) showed that the average oxidation state of Mo changed from ca. +4.8 to +0.9, corresponding to a shift in the Mo K-edge energy from 20013.5 to 20002.5 eV (Supplementary Figure 24). Overall, XPS and XANES results indicate a reduction of Mo sites in Mo₂CT_x in both H₂ treated materials, owing to a de-functionalization of the T_x groups at the MXene surface.

To investigate if the Mo state changes during the CO₂ hydrogenation reaction, we performed an operando XANES investigation at the Mo K-edge at 230 °C and under 10 bar of reactants, with the products measured simultaneously by a gas chromatography (GC). In agreement with the XPS results, operando XANES data shows no notable change in the oxidation state of Mo and its local environment with TOS (2 h), which is corroborated by a stable methanol STY and selectivity (Supplementary Figure 25). Results of the operando XANES experiment are consistent with laboratory catalytic tests and the observed stability within 24 h of TOS (Supplementary Figure 17).

The presence of Cu⁺ is identified in CuMes/Mo₂CT_x/SiO₂ owing to a low-intensity satellite feature at 942 eV in the Cu 2p XPS region (Supplementary Figure 26). While the H₂

treatment leads to the disappearance of this subtle feature, in line with the reduction of Cu^+ in the grafted species to metallic copper, the Cu L_3VV Auger region is more sensitive to Cu^+ sites identified at 915.2 eV (Fig. 2a and Supplementary Table 5)⁴⁴. Only a small fraction of less than 10% of Cu^+ sites is detected in $\text{Cu}/\text{SiO}_2\text{-2h}$, which is likely owing to the interfacial $\text{Cu-O-Si}\equiv$ sites, given the absence of C-H bands from the CuMes precursor in the IR spectrum of $\text{Cu}/\text{SiO}_2\text{-2h}$ (Fig. 1b). Instead, Cu is mostly present in $\text{Cu}/\text{SiO}_2\text{-2h}$ as a Cu^0 phase identified by a peak centered at 918.4 eV. On the contrary, increasing amounts of Cu^+ are observed in $\text{Cu}/\text{Mo}_2\text{CT}_x/\text{SiO}_2\text{-2h}$ and $\text{Cu}/\text{Mo}_2\text{CT}_x/\text{SiO}_2\text{-6h}$ (ca. 21 and 31%, respectively). Interestingly, the Cu^+ fraction grows with increasing reduction time (from 2 h to 6 h) and this occurs simultaneously with the decrease of Mo^{5+} states and increase of Mo^{4+} states. This reduction of Mo can be due to the deoxygenation of the surface oxygen in Mo_2CO_x oxycarbide 2D nanosheets by H_2 . However, because the increase in the fraction of Cu^+ sites (i.e., oxidation of metallic copper) occurs simultaneously with the reduction of molybdenum, it is likely that surface μ -oxo sites (Mo-O-Mo) of Mo_2CO_x interact with Cu^0 by forming Mo-O-Cu^+ linkages and thereby reduce Mo (Fig. 1a). The increase in the fraction of Cu^+ sites correlates with both the increasing catalytic activity and selectivity of the catalysts for CO_2 hydrogenation to methanol (i.e. $\text{Cu}/\text{SiO}_2\text{-2h} < \text{Cu}/\text{Mo}_2\text{CT}_x/\text{SiO}_2\text{-2h} < \text{Cu}/\text{Mo}_2\text{CT}_x/\text{SiO}_2\text{-6h}$). After 24 h of TOS, the amount of Cu^+ does not change significantly, indicating the stability of the Cu sites under reactive conditions (Supplementary Figures 27 and 28, Supplementary Table 5).

In addition to Mo K-edge XANES, Cu K-edge X-ray absorption spectroscopy (XAS) data were acquired during the in situ H_2 TPR capillary experiment described above, and showed a decrease of the edge position and white line intensity with heating; according to the Cu K-edge XAS data the formation of metallic Cu occurs at ca. 230 °C (Supplementary Figure 29). There is no significant change of the Cu state after the reduction of $\text{Cu}/\text{Mo}_2\text{CT}_x/\text{SiO}_2\text{-0.5h}$

(exposed to air and then treated under H₂ from RT to 500 °C) for 5.5 h at 500 °C (Supplementary Figure 30). Concerning the Cu K-edge XAS experiments, it is worth noting that at this stage we cannot exclude the reduction of Cu⁺ to metallic copper due to beam damage⁴⁵. Based on the fittings of the extended X-ray absorption fine structure (EXAFS) functions of Cu/Mo₂CT_x/SiO_{2-6h} and Cu/SiO_{2-2h} (Supplementary Figures 31–33), a shorter interatomic Cu–Cu distance is observed in Cu/Mo₂CT_x/SiO_{2-6h} (2.534(5) Å) compared with Cu/SiO_{2-2h} (2.519(4) Å) likely due to the small clusters of Cu on Mo₂CT_x, and thus higher dispersion of the Cu phase or due to different particle shapes⁴⁶ (Supplementary Table 6). Importantly, we observe no evidence of alloying of Cu with Mo, in contrast to what has been reported for the reduction of Pt on Ti- or Nb-based MXene^{31,32}. During the CO₂ hydrogenation reaction, the operando XAS data collected at the Cu K-edge shows no notable changes with TOS, indicating the stability of the Cu phase(s) under reaction conditions (Supplementary Figure 25 and Supplementary Table 6).

Next, to investigate the redox properties of Cu in the prepared materials, we compared the H₂ TPR behaviour of the materials after their oxidation by 5% O₂ at room temperature. The total amount of H₂ consumed to reduce the oxidized Cu/SiO_{2-2h} is consistent with the expected amount of H₂ based on the Cu loading determined by ICP (96%, Supplementary Table 1), indicating that most of the Cu sites in Cu/SiO_{2-2h} were oxidized to CuO and then reduced to metallic Cu with a maximum in the H₂ TPR profile at 168 °C (Fig. 2b). However, for Cu/Mo₂CT_x/SiO_{2-2h} oxidized in the same conditions, the H₂ consumption constitutes only 68% of the total Cu measured by ICP while the TPR profile shows a broader, unsymmetrical peak compared to that of oxidized Cu/SiO_{2-2h}, centered at a ca. 15 °C higher reduction temperature (Fig. 2b). This phenomenon is more pronounced for Cu/Mo₂CT_x/SiO_{2-6h}, which shows a maximum at a reduction temperature of 201 °C. In contrast, the reference material Mo₂CT_x/SiO_{2-2h} with the same Mo loading does not show notable H₂ consumption peaks in

the TPR after it has been oxidized. This data can be rationalized taking into account the increasing amount of Cu^+ sites in $\text{Cu}/\text{Mo}_2\text{CT}_x/\text{SiO}_2$ that has been exposed to a longer reductive pretreatment. It is likely that such Cu^+ sites are not oxidized by 5% O_2 at room temperature, which then accounts for the decreased consumption of H_2 in the TPR experiment. That being said, two other effects might contribute to the observed TPR results. First, it has been reported that Cu on $\beta\text{-Mo}_2\text{C}$ exhibits strong electronic metal-support interaction that leads to a partial charge transfer from Cu atoms to $\beta\text{-Mo}_2\text{C}$, which aids the high dispersion of copper²³. In addition, Cu might fill positions of Mo vacancies in the structure of Mo_2CT_x , similarly to what was reported for single Pt atoms confined in vacancies of $\text{Ti}_3\text{C}_2\text{T}_x$ ³⁴. At this stage, it is not clear to what extent these two alternatives play a role in the oxidation-reduction behaviour of the $\text{Cu}/\text{Mo}_2\text{CT}_x/\text{SiO}_2$ system.

Additional temperature-programmed desorption (TPD) of H_2 experiments allowed us to verify the different nature of the Cu sites in the prepared catalysts. While only one H_2 desorption peak is observed for $\text{Cu}/\text{SiO}_2\text{-2h}$ at 20 °C, two peaks are observed for $\text{Cu}/\text{Mo}_2\text{CT}_x/\text{SiO}_2\text{-2h}$ and $\text{Cu}/\text{Mo}_2\text{CT}_x/\text{SiO}_2\text{-6h}$ at 20 and 40 °C (Fig. 2c). This suggests that the desorption peaks at 20 and 40 °C are, respectively, due to Cu on the SiO_2 surface and Cu sites on Mo_2CT_x . Analysis of the relative peak areas indicates that the fraction of $\text{Cu}/\text{Mo}_2\text{CT}_x$ sites increased from 44% in $\text{Cu}/\text{Mo}_2\text{CT}_x/\text{SiO}_2\text{-2h}$ to 55% in $\text{Cu}/\text{Mo}_2\text{CT}_x/\text{SiO}_2\text{-6h}$ (Supplementary Table 7). The H_2 capacity of Cu/SiO_2 , $\text{Cu}/\text{Mo}_2\text{CT}_x/\text{SiO}_2\text{-2h}$ and $\text{Cu}/\text{Mo}_2\text{CT}_x/\text{SiO}_2\text{-6h}$, calculated from H_2 -TPD data, are 35.2, 18.1, and 9.5 $\mu\text{mol g}_{\text{cat}}^{-1}$, respectively (Supplementary Table 1). We explain this trend by the increasing fraction of surface Cu^+ sites with increasing duration of the reductive pretreatment, as was already discussed above.

Diffuse reflectance infrared Fourier transform spectroscopy (DRIFTS) using CO as the probe molecule was used to evaluate the electronic properties of the copper sites on the surfaces of

SiO₂ and Mo₂CT_x. Experiments were performed using a Praying Mantis reaction cell with in situ reduced materials (H₂, 500 °C) that were then exposed to 10% CO/N₂ for 10 min and flushed with N₂ for 60 min at room temperature. Under these conditions, CO desorbs from weakly bound CO–Cu⁰ adducts³⁷, while stronger bound CO–Cu⁺ adducts remain present. Upon binding of CO, a main peak at 2124 cm⁻¹ and a shoulder at 2112 cm⁻¹ are observed for Cu/SiO_{2-2h} (Fig. 2d), consistent with previous studies⁴⁷. The intensity of the peaks of adsorbed CO on Cu/SiO_{2-2h} decreases at 100 °C and the peaks eventually disappear at 200 °C in N₂ flow due to the desorption of CO. However, in both Cu/Mo₂CT_x/SiO₂ catalysts, there is an additional blue-shifted feature at 2134 cm⁻¹ and its intensity is higher for Cu/Mo₂CT_x/SiO_{2-6h} than for Cu/Mo₂CT_x/SiO_{2-2h}. The peak at 2134 cm⁻¹ is observed even at 200 °C, in contrast to the bands at 2124 and 2112 cm⁻¹ attributed to CO–Cu⁺ adducts on Cu/SiO_{2-2h}. Note that without Cu, Mo₂CT_x/SiO_{2-2h} does not absorb CO at room temperature (Supplementary Figure 35). The CO adsorption peak at 2134 cm⁻¹ is ascribed therefore to the presence of Cu⁺ sites on Mo₂CT_x^{48,49}. An alternative explanation that, however, appears less likely is that highly dispersed metallic Cu (vacancy-confined single Cu atoms in the lattice of Mo₂CT_x or small Cu clusters in the electronic interaction with the support) give more stable CO adducts. The higher stability of CO–Cu⁺ adducts relative to CO–Cu⁰ is due to the stronger σ-donation from the highest occupied molecular orbital (HOMO) of CO to the more Lewis acidic (relative to metallic Cu) Cu⁺ sites^{44,50}. Depletion of electron density from the slightly antibonding HOMO of CO leads to the observed blue shift and strengthens the CO–Cu⁺ interaction, while the π-backbonding interaction may be only slightly reduced in CO–Cu⁺ relative to that in CO–Cu⁰ adducts^{44,51}. It is likely that the enhanced activity of Cu/Mo₂CT_x/SiO_{2-6h} in CO₂ hydrogenation is due to the Cu⁰/Cu⁺/Mo₂CT_x interface, which is reminiscent of the Cu⁰/Cu⁺/CeO_{2-x} interface reported recently⁴⁴. Overall, the CO DRIFTS results (after the desorption of CO from Cu⁰ sites in N₂ flow) are consistent with the presence

of Cu^+ sites that bind CO strongly (band at 2134 cm^{-1}) in $\text{Cu}/\text{Mo}_2\text{CT}_x/\text{SiO}_2$ material, assigned to Cu^+ on Mo_2CT_x nanosheets. The peak positions of CO adsorbed on Cu^+ sites are unchanged in $\text{Cu}/\text{Mo}_2\text{CT}_x/\text{SiO}_2\text{-2h}$ and $\text{Cu}/\text{Mo}_2\text{CT}_x/\text{SiO}_2\text{-6h}$. Overall, Cu XPS (Auger peaks), H_2 TPR, H_2 TPD, and CO DRIFTS data suggests that a longer thermal treatment in H_2 at $500\text{ }^\circ\text{C}$ (6 h vs. 2 h) unexpectedly results in a higher fraction of Cu^+ sites on the Mo_2CT_x phase, which proceeds in parallel with the reduction of Mo sites in Mo_2CT_x . Thus, while the atomically thin Mo_2CT_x nanosheet support is reducible³⁰, it lacks the typical SMSI overcoating effect of typical metal oxide supports (bulk or nanoparticles, e.g. TiO_2 , CeO_2 , ...). Therefore, as the Cu^0/Cu^+ interface appears to be related on CeO_2 and on Mo_2CT_x , it is the absence of an encapsulation of the active phase by the reduced support on rigid, thermally stable Mo_2CT_x nanosheets³⁰, which do not change their 2D morphology with TOS (vide infra), that is likely responsible for the improved catalytic performance of $\text{Cu}/\text{Mo}_2\text{CT}_x/\text{SiO}_2$.

Nature of Cu sites from $\text{Cu}/\text{Mo}_2\text{CO}_x$ models

Periodic density functional theory (DFT) calculations using the BEEF-vdW density functional⁵² were carried out to improve our understanding of the nature of Cu sites in $\text{Cu}/\text{Mo}_2\text{CT}_x/\text{SiO}_2\text{-2h}$ and $\text{Cu}/\text{Mo}_2\text{CT}_x/\text{SiO}_2\text{-6h}$ catalysts and to refine the possible interaction between Cu and Mo_2CO_x nanosheets. A 3×3 -unit cell derived from a Mo_2C (001) surface slab containing two Mo layers, one at the top and one at the bottom of the slab, and one middle carbon layer, in agreement with the stoichiometry of the material, was used to model the Mo_2CO_x surface. A further description of the methodology and details of the Mo_2C model³⁰ as well as the reference Cu (111) and Cu_2O (111) surfaces can be found in Supplementary Figures 36 and 37. First, we supported one and four Cu atoms on the 3×3 2D- Mo_2C surface to generate the respective $\text{Cu}/2\text{D-Mo}_2\text{C}$ (Model 1) and $\text{Cu}_4/2\text{D-Mo}_2\text{C}$ (Model 1b) surface structures. In addition, we considered the following oxygen coverages for one supported Cu atom: $2/9$, $5/9$,

6/9 and 7/9 of a full oxygen monolayer (ML), denoted Model 2, 3, 4 and 5, respectively. These different oxygen coverages model various oxidation states of the Mo_2CO_x nanosheets of the experimental system, as was determined by the XANES and XPS analyses of the $\text{Cu}/\text{Mo}_2\text{CT}_x/\text{SiO}_2\text{-2h}$ and $\text{Cu}/\text{Mo}_2\text{CT}_x/\text{SiO}_2\text{-6h}$ catalysts discussed above.

First, we compared energies of hydrogen adsorption on the Cu (111) slab, $\text{Cu}/2\text{D-Mo}_2\text{C}$, $\text{Cu}_4/2\text{D-Mo}_2\text{C}$ and $\text{Cu}/2\text{D-Mo}_2\text{C-0.67 O ML}$ (i.e. Model 4) by evaluating the dissociative adsorption of H_2 forming atomic hydrogen species (H^*). On Cu (111), H^* adsorbs on the hcp hollow site (Supplementary Figure 38), while on $\text{Cu}/2\text{D-Mo}_2\text{C}$, $\text{Cu}_4/2\text{D-Mo}_2\text{C}$, and $\text{Cu}/2\text{D-Mo}_2\text{C-0.67 O ML}$ (Models 1, 1b, and 4), H^* adsorbs on the $\text{Cu}/2\text{D-Mo}_2\text{C}$ interface with the respective electronic binding energies of -0.3 , -34 , -28 , and -27 kJ mol^{-1} with respect to the gas-phase H_2 molecule, i.e. a stronger H^* adsorption is observed on all evaluated $\text{Cu}/2\text{D-Mo}_2\text{C}$ interfaces in comparison to the Cu (111) slab (Fig. 2e–g). These results show that the interface in $\text{Cu}/2\text{D-Mo}_2\text{C}$, $\text{Cu}_4/2\text{D-Mo}_2\text{C}$ or $\text{Cu}/\text{Mo}_2\text{CO}_x$ surfaces can be responsible for the stronger hydrogen adsorption, in agreement with the H_2 TPD results (Fig. 2c) that revealed a higher temperature for H_2 desorption for the $\text{Cu}/\text{Mo}_2\text{CT}_x$ catalysts relative to the Cu/SiO_2 reference catalyst (represented by the Cu (111) slab model in our DFT calculations). Yet, Model 4 represents our experimental systems better than Model 1, because Mo is oxidized in the $\text{Cu}/\text{Mo}_2\text{CT}_x/\text{SiO}_2$ catalysts according to XANES and XPS results described above.

Next, we found that CO adsorbs preferentially atop of Cu in Models 1–5 featuring binding energies of -62 , -77 , -70 , -89 , and -83 kJ mol^{-1} for Models 1 to 5, respectively (Fig. 2h and i). According to the Bader charge analysis, Cu atoms with an adsorbed CO molecule in Models 4 and 5 have oxidation states of $+0.6$ and $+0.5$, i.e. in these models Cu sites have the most significant $\text{Cu}^{\delta+}$ character (Supplementary Figure 39), which correlates also with a higher CO binding energy and a stronger blue shift of vibrational frequency of CO with respect to

Cu/2D-Mo₂C (Supplementary Table 9). The Cu^{δ+} character becomes more notable upon CO adsorption (Supplementary Figure 39). We calculated the stretching frequency of CO on Cu (111) and Cu₂O (111) reference surfaces and found that CO on the Cu (111) surface is red-shifted (2020 cm⁻¹) and CO on the Cu₂O (111) surface is blue-shifted (2093 cm⁻¹, Supplementary Table 9). The latter frequency is comparable to the frequency of adsorbed CO in Models 4 and 5. This is consistent with the high Cu^{δ+} character found using the Bader charge analysis for Cu sites in Models 4 and 5.

The calculated shift of the CO stretching frequency with respect to gas-phase CO is -38 cm⁻¹ for Model 4 and -30 cm⁻¹ for Model 5 (BEEF-vdW functional). When evaluated using the PBE0 functional, the calculated shift for Model 4 is -18 cm⁻¹, which is close to the experimental shift of -9 cm⁻¹ (Supplementary Table 10). Overall, we conclude that Cu sites in Models 4 and 5 have a significant Cu^{δ+} character, consistent with experimental results.

Characterization of reaction intermediates

Two mechanistic pathways for CO₂ hydrogenation to methanol were proposed, *viz.* involving CO or formate as intermediates^{17,53}. Our contact time experiments have identified CO and methanol as the primary products of CO₂ hydrogenation (Supplementary Figures 6 and 7, Supplementary Table 2); therefore intermediacy of CO in the formation of methanol is unlikely¹³. To explore the surface intermediates of CO₂ hydrogenation over the Cu/Mo₂CT_x/SiO₂ catalysts, we relied on an operando DRIFTS study with the simultaneous quantification of products by gas chromatography. At 230 °C and 25 bar (H₂/CO₂/N₂ = 3/1/1), formate (2936, 2857, and 2698 cm⁻¹) and methoxy peaks (2996 and 2959 cm⁻¹)^{13,54} are identified on Cu/Mo₂CT_x/SiO_{2-2h}, while carbonate or bicarbonate peaks are not observed (Fig. 3a and Supplementary Figure 40). The intensity of the bands owing to surface formate groups and the STY of methanol reaches a steady state after ca. 60 min of TOS, whereas the

intensity of peaks due to surface methoxy groups continues to increase for a substantially longer time, ca. 15 h. The amplitude of the bands due to surface formate and methoxy grows faster for Cu/Mo₂CT_x/SiO_{2-2h} than for Cu/SiO_{2-2h}, which correlates with a higher STY of methanol, as quantified by GC (Fig. 3b).

Note that the formate peaks are more intense on Cu/Mo₂CT_x/SiO_{2-2h} than on Cu/SiO_{2-2h} at lower pressures (≤ 20 bar), including under atmospheric pressure (Supplementary Figure 41). The trend for the formation of a carbonyl band at 2077 cm⁻¹ (i.e. intermediate for CO) at different pressures is the opposite to that of formate, indicating the selective formation of methanol on the Cu/Mo₂CT_x/SiO₂ catalyst compared to Cu/SiO₂ (Supplementary Figure 41). To verify that the formate species are intermediates on the methanol synthesis pathway, Cu/Mo₂CT_x/SiO_{2-2h} was exposed to a H₂/CO₂/N₂ (3/1/1) feed for 10 min at atmospheric pressure and then the CO₂ flow was discontinued. The surface formate bands decreased gradually while methanol was detected by GC (Supplementary Figure 42), implying that formate species could be hydrogenated by H₂ on Cu/Mo₂CT_x/SiO_{2-2h} to methanol.

To further explore the nature of the reaction intermediates, we used solid-state ¹³C NMR spectroscopy. This method provides primarily information on adsorbed intermediates on the support since intermediates on metallic copper can suffer from signal broadening and Knight shifts¹³. Cu/Mo₂CT_x/SiO_{2-2h} was kept under 5 bar of ¹H₂/¹³CO₂ (3/1) at 230 °C for 12 h followed by outgassing at room temperature and ssNMR analysis. The observed ¹³C NMR chemical shift at 172 ppm is consistent with the presence of formate species (Fig. 3c), which is however not observed in ¹H NMR, probably due to a too weak or broad signal (Supplementary Figure 43). The formate peak is more deshielded on Cu/Mo₂CT_x/SiO_{2-2h} (172 ppm) than on Cu/SiO₂ (168 ppm)¹³. Species with the ¹³C chemical shift at 49 ppm and ¹H NMR chemical shift at 3.9 ppm are ascribed to surface -OCH₃ species (possibly, Cu-

OCH₃). Note that these signals have not been observed on Cu/SiO₂ in the absence of Mo₂CT_x¹³ after reaction under 5 bar of ¹H₂/¹³CO₂ (3/1), yet operando DRIFTS at 25 bar reveals methoxy bands on Cu/SiO₂ (Fig. 3b). No intermediates are observed on Mo₂CT_x/SiO₂. Therefore, neither Cu NPs alone nor Mo₂CT_x alone can generate methoxy species from formate species under the conditions used for the ¹³C NMR experiments (i.e. 230 °C and 5 bar) and it is the Cu dispersed on Mo₂CT_x nanosheets that yields the surface methoxy species. Furthermore, also formate species are not observed on Mo₂CT_x/SiO₂ (Fig. 3c).

DFT-computed reaction pathways over single atom Cu/Mo₂CO_x

We performed DFT calculations using the BEEF-vdW functional⁵² to obtain atomic-level insight into the pathway of CO₂ hydrogenation to methanol or CO on the Cu/2D-Mo₂C-0.67 O ML surface (this model has been described above in Fig. 1g). This particular structure was selected as a realistic model for the DFT calculations and used to evaluate the respective energy profiles to form methanol or CO (Fig. 4). In what follows, we describe the most probable reaction pathways and aim to rationalize the experimental observations.

As oxygen covers only partially the 2D-Mo₂C surface in our model, reactive Mo sites with a proximal Cu atom are accessible. The interaction of CO₂ and H₂ on the model surface is exoenergetic by merely 14 kJ mol⁻¹, suggesting that both species are physisorbed, as also inferred from the very minor changes of the geometries of CO₂ and H₂ upon their interaction with the surface. These two physisorbed molecules then form formate (HCOO*) and adsorbed H*. This step proceeds via a transition state TS1, associated with an energy barrier of 103 kJ mol⁻¹, which we interpret as the CO₂-assisted heterolytic cleavage of H₂. In TS1, CO₂ is significantly bent ($\angle\text{O-C-O}$ is ca. 125°) with one O pointing to Mo. The H₂ molecule is cleaved in TS1 heterolytically, i.e. forming simultaneously new C-H and Cu-H bonds. Since

both CO₂ and H₂ do not chemisorb on 2D-Mo₂C-0.67 O ML for this step, it can be classified as Eley-Rideal type⁵⁵. Note that HCOO* species have been detected by DRFITS and ¹³C MAS NMR spectroscopies (Fig. 3). The resulting formate intermediate (**2**, Fig. 4) is η²-coordinated at the Cu/2D-Mo₂C-0.67 O ML interface such that one O of the formate is coordinated to Cu and the second O is coordinated to Mo. The H* atom is also adsorbed at the Cu/2D-Mo₂C-0.67 O ML interface. HCOO* species can re-orient to coordinate both of its oxygen atoms to surface Mo in a low energy process via TS2 (52 kJ mol⁻¹), likely due to the higher oxophilicity of Mo compared to Cu. This migration of the HCOO* species on the 2D-Mo₂C-0.67 O ML surface allows to stabilize the dioxymethylene species (H₂COO*, **5**, Fig. 4), as discussed below.

Previous DFT pathways of the hydrogenation of CO₂ to methanol on Cu or Cu-alloy surfaces proposed that the formation of H₂COOH* from HCOO* species proceeds through formic acid (HCOOH*)³. In contrast, on a Cu/2D-Mo₂C-0.67 O ML surface, we have identified a pathway leading to the formation of H₂COO* from HCOO* species, with similar energetics as in the literature³, which includes the H-transfer to the η²-coordinated formate via TS3. In this transition state, H₂ is cleaved heterolytically yielding H₂COO* and H* species, that is forming C–H and Cu–H bonds in a pathway similar to TS1 discussed above. TS3 has the highest energy barrier (141 kJ mol⁻¹) in the pathway of CO₂ hydrogenation to methanol, i.e. it is the rate-limiting transition state. The most favorable pathway to methanol from the H₂COO* and H* species proceeds through formaldehyde (H₂CO*) and hydroxy (OH*) species (**6**, Fig. 4). This pathway involves both the cleavage of the C–O bond of H₂COO* as well as the formation of OH* species. It has been postulated that H₂ assistance is required for C–O bond cleavage on Cu/Mo₂C surfaces²⁴. Yet on the Cu/2D-Mo₂C-0.67 O ML model surface, the formation of co-adsorbed H₂CO* and OH* proceeds with a very low energy barrier of 16 kJ mol⁻¹ (TS4). In a subsequent TS5, with an energy barrier of 37 kJ mol⁻¹, H-transfer from OH* to H₂CO* leads

to methoxy (CH_3O^*) and O^* (**7**). The intermediate structure **7** is located at -273 kJ mol^{-1} and this high stability explains the observation of these species in FTIR and NMR experiments as described above. The regeneration of the OH^* species proceeds by the reaction of H^* with the O^* atom at the interface between Cu and 2D-Mo₂C-0.67 O ML. This TS6 has an energy barrier of 89 kJ mol^{-1} . The last step generates methanol by proton transfer from the OH^* group to OCH_3^* via TS7, requiring 57 kJ mol^{-1} . The resulting CH_3OH^* species (**9**) is located at -243 kJ mol^{-1} in the energy diagram. Methanol desorption requires 87 kJ mol^{-1} . Finally, the adsorbed O^* atom leads to the formation of water in a pathway that is shared with the RWGS reaction and explained in detail in the following section.

We note that starting from the H_2COO^* species, three alternative reaction pathways to form methanol are possible, which are however energetically less favorable than the pathway presented in Fig. 4. Two pathways involve the formation of H_2COOH^* as a reaction intermediate, while the third pathway features the direct C–O cleavage of H_2COO^* , forming formaldehyde (H_2CO^*) and O^* in a single step. These pathways are discussed in Supplementary Figures 45–48.

We have also evaluated the energy profile of the competitive reverse water–gas shift reaction using the Cu/2D-Mo₂C-0.67 O ML model (Fig. 4). The adsorption of CO_2 (in the absence of H_2) on the surface is exoenergetic by 18 kJ mol^{-1} (**11**) and leads to a bent CO_2 (**12**, $\angle\text{O–C–O}$ is ca. 136°) at the interface of the Cu atom and the 2D-Mo₂C-0.67 O ML surface via TS8 with an energy barrier of 35 kJ mol^{-1} . From intermediate **12**, C–O bond cleavage has a very low energy barrier of 3 kJ mol^{-1} (TS9). Thus, CO^* is readily formed by the direct activation of CO_2 adsorbed at the Cu/2D-Mo₂C-0.67 O ML interface yielding CO^* and O^* species. CO^* adsorbed on a Cu atom (**13**) is located at -109 kJ mol^{-1} and desorption of CO from Cu in intermediate **13** requires 80 kJ mol^{-1} . This pathway to CO features relatively low activation

barriers compared to the methanol formation route, and is consistent with the experimentally observed formation of CO, along with methanol, in our catalytic tests. Following the desorption of CO, H₂ is adsorbed on the Cu atom, which is energetically favorable by 13 kJ mol⁻¹ (**15**). In this intermediate **15**, H₂ is coordinated to Cu in a η² mode with a H–H distance of 0.759 Å, and with respective Cu–H distances of 1.95 Å and 1.97 Å. In the next step, the heterolytic cleavage of H₂ yields simultaneously O–H and Cu–H bonds, forming intermediate **16**. This step is endoenergetic by 29 kJ mol⁻¹ with an energy barrier in TS10 of 73 kJ mol⁻¹. Finally, H₂O* forms by the subsequent reaction of OH* with H* on the Cu/2D-Mo₂C-0.67 O ML interface with an energy barrier of 100 kJ mol⁻¹ (in TS11), i.e. the rate-limiting step of the RWGS pathway. The resulted intermediate **17** is located 3 kJ mol⁻¹ higher than the initial reactants. The final step i.e. the desorption of water is endoenergetic and requires 65 kJ mol⁻¹.

We have also evaluated an alternative RWGS mechanism involving the activation of H₂ to form 2H* on the Cu/2D-Mo₂C-0.67 O ML interface. This process, however, involves a high energy barrier of 144 kJ mol⁻¹ and is endoenergetic by 72 kJ mol⁻¹ (Supplementary Figure 49), which makes it energetically less favorable compared to the route described above. Overall, the presented RWGS mechanism (Fig. 4), including the heterolytic cleavage of H₂, proceeds via the chemisorption of each reactive species and therefore follows a Langmuir-Hinshelwood type manifold⁵⁶ on our Cu/2D-Mo₂C-0.67 O ML model, in contrast to the CO₂ hydrogenation pathway discussed above.

To summarize, DFT calculations highlight the likely intermediates and transition states and allow to propose a feasible energy profile for the pathways of CO₂ hydrogenation to methanol and CO on a Cu/2D-Mo₂C-0.67 O ML model. The interface between a Cu atom and the 2D-Mo₂C-0.67 O ML surface plays a crucial role in the CO₂ hydrogenation reactions. The Cu atom and the support both participate in the reaction mechanism by reducing the

energy barriers for successive heterolytic cleavages of H₂ that are required to form HCOO*, H₂COO*, and H₂COOH* species, simultaneously with adsorbed H*. The most energy-demanding step in the methanol production pathway is the formation of the H₂COO* species. The Cu/2D-Mo₂C-0.67 O ML interface also provides a low energy route for CO₂ adsorption, followed by its direct cleavage into CO* and O*. Hence, on the Cu/2D-Mo₂C-0.67 O ML model, both CH₃OH and CO are easily obtained under CO₂ hydrogenation conditions, providing an explanation for the experimental observation of both products. Finally, the most strongly adsorbed reaction intermediates determined by our DFT calculations are HCOO* and CH₃O*, that is the same intermediates that are observed in our operando DRIFTS and NMR experiments.

CONCLUSIONS

In conclusion, our work demonstrates that highly dispersed Cu species, including single Cu atoms, can be enriched selectively on the Mo₂CT_x phase by migration from SiO₂ under reductive pretreatment. Consequently, the Cu/Mo₂CT_x/SiO₂ catalysts show two different Cu sites: Cu/Mo₂CT_x and Cu/SiO₂. The Cu/Mo₂CT_x interface, with Lewis acidic Cu⁺ sites, is responsible for the observed increased methanol formation rate and selectivity. These findings, complemented by DFT calculations, show the prospects of copper single atom catalysis for CO₂ hydrogenation exploiting metal-support interactions in general and Cu/MXenes interfaces in particular.

Methods

Catalyst preparation

SiO₂ (Aerosil 300) was compacted, sieved (180–300 μm), and calcined in static air (500 °C, 3 h). The calcined material had a surface area of 374 m² g⁻¹ and a pore volume of 2.0 mL g⁻¹.

Mo₂Ga₂C was synthesized as reported previously²⁸ and treated in a 14 M HF solution at 55 °C for 7 days in a sealed Teflon-lined autoclave⁴². This gave a mixture of Mo₂CT_x and Mo₂Ga₂C phases that was washed and dried (Supplementary Figure 50). Ca. 2 g of this material was dispersed in 30 mL of 40% tetrabutylammonium hydroxide (TBAOH) and 10 mL of water and stirred at room temperature for 12 h. The solid was then separated via centrifugation (6000 rpm, 5 min) and washed with ethanol (2 × 40 mL) and water (3 × 40 mL), followed by sonication (40 min) and centrifugation (3500 rpm, 30 min). The supernatant containing colloidal solution of delaminated 2D-Mo₂CT_x nanosheets was collected (Supplementary Figure 1). Ca. 150 mL of this 2D-Mo₂CT_x solution was impregnated onto 5 g SiO₂ using incipient wetness impregnation (15 cycles of impregnation and drying under vacuum at 50 °C for 4 h). No Ga signal was observed in the X-ray photoelectron spectroscopy (XPS) of Mo₂CT_x/SiO₂ (Supplementary Figure 51), indicating that 2D-Mo₂CT_x was separated from the bulk Mo₂Ga₂C during centrifugation.

Mo₂CT_x/SiO₂ was dehydroxylated under a N₂ flow (20 mL min⁻¹, with O₂ and moisture traps) at 500 °C for 12 h with a heating rate of 1 °C min⁻¹. The sample was then cooled down under high vacuum (10⁻⁵ mbar) for 1 h and handled in a glovebox (material referred to as Mo₂CT_x/SiO₂₋₅₀₀). The surface density of hydroxyl groups of the support was determined by chemical titration using an excess of [Mg(CH₂Ph)₂(THF)₂] as a reactant, while monitoring the extent of the reaction by ¹H NMR (d1 = 60s) using ferrocene as an internal standard³⁶. Cu/Mo₂CT_x/SiO₂ was prepared via a surface organometallic chemistry approach using [Cu₅(Mesityl)₅] (Strem Chemicals)^{12,37}. In a glovebox, Mo₂CT_x/SiO₂₋₅₀₀ (1 g, 0.47 mmol of ≡SiOH sites) was dispersed in 5 mL of dry toluene and contacted with a solution of [Cu₅(Mesityl)₅] (72 mg, 0.39 mmol of Cu) in 5 mL of toluene. The reaction mixture was stirred at 100 rpm for 3 h at room temperature. After the grafting, the solid was washed with

toluene (3×5 mL) and dried (10^{-5} mbar) at room temperature for 3 h. Before catalytic tests, the grafted material was reduced under H_2 (50 mL min^{-1}) at $500 \text{ }^\circ\text{C}$ for 2 h or 6 h (Cu/Mo₂CT_x/SiO_{2-2h} and Cu/Mo₂CT_x/SiO_{2-6h}, respectively). A reference Cu/SiO_{2-2h} catalyst was prepared by the same procedure.

The industrial methanol synthesis catalyst (Alfa Aesar) contains 63.5 wt% CuO, 25 wt% ZnO, 10 wt% Al₂O₃, and 1.5 wt% MgO fume. In addition, a Cu-ZnO-Al₂O₃ catalyst with 2.5 wt% Cu, 12.5 wt% ZnO, and 85.0 wt% Al₂O₃ was synthesized by a conventional co-precipitation route^{5,7}. More specifically, Cu(NO₃)₂·2.5H₂O (183 mg, 0.8 mmol), Zn(NO₃)₂·6H₂O (910 mg, 3.0 mmol), and Al(NO₃)₃·9H₂O (6259 mg, 16.7 mmol) were dissolved in deionized water to make a 1 M solution. The solution was then titrated with 1 M Na₂CO₃ to reach the pH of 8.0. The precipitate was filtered and washed with deionized water until pH 7.0 was reached. Subsequently, the precipitate was dried at $90 \text{ }^\circ\text{C}$ overnight and calcined at $350 \text{ }^\circ\text{C}$ for 12 h. The Cu-ZnO-Al₂O₃ catalysts were reduced under H_2 at $250 \text{ }^\circ\text{C}$ for 3.5 h according to the published protocols^{3,5} (denoted Cu-ZnO-Al₂O_{3-com-250} and Cu-ZnO-Al₂O_{3-syn-250}) or at $500 \text{ }^\circ\text{C}$ for 6 h, according to the protocol for the synthesis of Cu/Mo₂CT_x/SiO_{2-6h} in this study (denoted Cu-ZnO-Al₂O_{3-com-250} and Cu-ZnO-Al₂O_{3-syn-250}). The characterization of these catalysts is shown in Supplementary Figures 52–57.

Catalyst characterization

The surface area and pore volume of the materials were determined by N₂ physisorption (Quantachrome NOVA 4000e) with the Brunauer-Emmet-Teller (BET) model (using the adsorption data) and Barrett-Joyner-Halenda (BJH) model (using the desorption data), respectively. Prior to the measurement, the samples were outgassed at $250 \text{ }^\circ\text{C}$ for 2.5 h. The Mo and Cu loadings of the catalysts were determined by inductively coupled plasma optical

emission spectroscopy (ICP-OES) using an Agilent 5100 VDV after digestion in aqua regia. Fourier-Transform Infrared (FTIR) spectroscopy experiments were performed on self-supporting wafers using a Bruker Alpha spectrometer in transmission mode (24 scans, 4 cm⁻¹ resolution) under a N₂ atmosphere. Intensities were normalized to the Si-O-Si overtones of the silica support. Powder X-ray diffraction (XRD) data were collected on a PANalytical Empyrean X-ray diffractometer equipped with a Bragg-Brentano HD mirror operated at 45 kV and 40 mA using Cu K α radiation ($\lambda = 1.5418 \text{ \AA}$). The materials were examined within the 2θ range of 5-90° using a step size of 0.0167°. The scan time per step was 3 s. X-ray photoelectron spectroscopy (XPS) measurements were conducted on a Sigma 2 instrument (Thermo Fisher Scientific) equipped with a UHV chamber (nonmonochromatic 200 W Al K α source, a hemispherical analyzer, and a seven-channel electron multiplier). The analyzer-to-source angle was 50°, whereas the emission angle was 0°. A pass energy of 50 and 25 eV was set for the survey and the narrow scans, respectively, and the C 1s peak of adventitious carbon was set at 284.8 eV to compensate for any charge-induced shift. An air-tight cell allowing to transfer specimens between the glovebox and the XPS instrument was used⁵⁷.

X-ray absorption spectra at the Cu and Mo K-edge were measured at the SuperXAS beamline at the Swiss Light Source (SLS), operating in top-up mode at a 2.4-GeV electron energy and a current of 400 mA. Cu XAS spectra were collected at the K-edge using a Si (111) monochromator in transmission mode with continuous scanning between 8760 and 10290 eV with a step size of 0.1 eV. Mo XAS spectra were collected at the K-edge in fluorescence mode (Si drift detector) with continuous scanning between 19800 and 21150 eV with a step size of 0.25 eV. Calibration of the monochromator energy position was performed by setting the inflection point of a Cu or Mo foil spectrum recorded simultaneously with the sample to 8979 or 20000 eV for Cu or Mo K-edges, respectively. In a typical operando experiment, 4 \pm 0.05 mg of the sample (Cu/Mo₂CT_x/SiO_{2-0.5h}) was packed into a quartz capillary reactor cell

(1.5 mm outer diameter, 0.02 mm wall thickness), which was connected with a pressurizable gas flow system. The catalysts went through the following steps: (i) heating to 500 °C under H₂ (1 bar, 10 mL min⁻¹, 10 °C min⁻¹) and holding for 5.5 h, (ii) cooling down to reaction temperature (230 °C) and pressurizing to 10 bar N₂, and (iii) switching to a CO₂ hydrogenation atmosphere (H₂/CO₂/N₂ = 3/1/1, 10 mL min⁻¹, 10 bar, space velocity = 150000 L kg⁻¹ h⁻¹) and holding for 2 h. The outlet of the capillary reactor was kept at 150 °C and fed into a GC (CompactGC, Global Analyser Solutions, equipped with thermal conductivity and flame ionization detectors) with a data sampling interval of 7 min. The ex situ samples of air-sensitive CuMes/Mo₂CT_x/SiO₂ and Cu/Mo₂CT_x/SiO_{2-6h} were sealed in the capillary in the glovebox and analyzed without exposure to air. Non-air-sensitive references were pressed into wafers with an optimized amount of sample mixed with cellulose and sealed in Kapton tape. The processing of the XAS data was performed with ProQEXAFS and the Athena software^{58,59}, and the EXAFS fittings were conducted with the Artemis software⁵⁹.

Transmission electron microscopy (TEM), scanning transmission electron microscopy (STEM) with a high-angle annular dark-field (HAADF) detection, and energy-dispersive X-ray (EDX) spectroscopy were carried out on an FEI Talos F200X transmission electron microscope. An aberration-corrected JEOL JEM-ARM300F Grand ARM scanning transmission electron microscope operated at 300 kV was also used with an air-tight sample holder. The microscope was equipped with the Dual EDS system (two large area SDD EDX detectors with 100 mm² active area; total solid angle: 1.6 sr). Gold grids were used. Scanning electron microscopy (SEM) measurements were performed on an FEI Magellan 400 FEG microscope. Prior to imaging, the samples were sputter-coated with a ca. 5 nm thick layer of PtPd (CCU-010 Metal Sputter Coater Safematic).

H₂ TPD and TPR experiments were performed using an AutoChem (Micromeritics) system with a thermal conductivity detector (TCD). In a typical H₂ TPD experiment, ca. 50 mg of the as-prepared material was loaded in air and reduced at 500 °C under H₂ flow (50 mL min⁻¹) for the specified time. Subsequently, the sample was purged with Ar for 30 min at 500 °C and cooled down to -50 °C under Ar. The sample was then saturated in 5% H₂/Ar flow for 30 min and purged with Ar for another 30 min. Finally, the sample was heated to 500 °C at 10 °C min⁻¹ under Ar flow and the desorbed H₂ was monitored with the TCD detector. For N₂O titration measurements, specimens were first pretreated under H₂ at 500 °C, followed by purging and cooling down to 50 °C under Ar. The gas was then switched to 5% N₂O/Ar for 60 min to oxidize the surface Cu⁰ sites to Cu⁺ and then reduced with 5% H₂/Ar from room temperature to 500 °C (10 °C min⁻¹). Similarly, the TPR experiments were carried out under 5% H₂/Ar from room temperature to 500 °C after the sample was oxidized by 5% O₂/He at room temperature.

DRIFTS measurements were performed using a Nicolet 6700 FTIR with a Praying Mantis (Harrick) high-pressure reaction chamber. A mercury cadmium telluride (MCT) detector was used. Catalysts were pelletized before the measurements and the spectra were recorded in the range of 4000-600 cm⁻¹ by averaging 64 scans with the resolution of 4 cm⁻¹. For CO adsorption and desorption, the sample was loaded in air and pretreated with pure H₂ at 500 °C (50 mL min⁻¹) for a specified period of time. After cooling down to room temperature, the specimen was exposed to 10% CO/N₂ flow (50 mL min⁻¹) for 10 min, with spectra collected every two minutes. Then the CO flow was stopped and spectra were collected under flowing N₂ for 60 min. The temperature was then increased to 100 °C and 200 °C at a heating rate of 10 °C min⁻¹. The background spectra were collected under N₂ at the corresponding temperatures. DRIFTS coupled with a GC-based gas analysis (CompactGC, Global Analyser

Solutions, equipped with thermal conductivity and flame ionization detectors) was used for the CO₂ hydrogenation reactions (i.e. in operando mode). After pretreatment with H₂ at 500 °C, the sample was cooled to 230 °C under N₂. The DRIFT spectrum recorded under N₂ flow at 230 °C and 25 bar was used as the background spectrum. CO₂ hydrogenation was carried out at 230 °C and 25 bar using a gas mixture of H₂/CO₂/N₂ = 3/1/1 and the spectra were recorded every 2 min. The product was analyzed by the GC every 7 min. The transfer line was kept at 150 °C to prevent product condensation. The DRIFT spectra were also collected at different reaction pressures (1, 2, 3, 5, 10, 15, 20, and 25 bar) following a similar procedure.

The solid-state NMR experiments on ¹H and ¹³C were recorded on a Bruker 400 MHz AVANCE III HD spectrometer with a 4 mm MAS triple resonance probe operating in double resonance mode with a magic angle spinning frequency of 10 kHz. The 35 kHz SPINAL64 decoupling was applied on the ¹³C-channel during acquisition⁶⁰. The chemical shift scale was calibrated using adamantane as an external secondary reference. Before the measurements, the catalysts were exposed to 5 bar ¹H₂/¹³CO₂ (3/1) at 230 °C for 12 h in a batch reactor, followed by the evacuation of the gas phase at room temperature under high vacuum (10⁻⁵ mbar).

CO₂ hydrogenation reactions

The CO₂ hydrogenation reactions were performed in a fixed-bed, tubular reactor (304.8 mm total length, 9.1 mm internal diameter, Hastelloy X, Microactivity Effi, PID Eng&Tech)⁶¹. In a typical experiment, the catalyst (100 mg) was first pretreated under H₂ at 500 °C for a specific time. The reaction was performed at 230 °C under 25 bar. The gas flow of H₂/CO₂/N₂ (3/1/1) (N₂ as internal standard) was passed through the catalyst bed and the

products were analyzed online by a GC (PerkinElmer Clarus 580) equipped with thermal conductivity and flame ionization detectors, and a methanizer. Different contact times (space velocities) were probed by changing the gas flow rate from 100 to 15 NmL min⁻¹. Finally, activity data were collected at the initial flow rate of 100 NmL min⁻¹ to check for potential deactivation of the catalyst. The formation rate, CO₂ conversion, and methanol selectivity were calculated using the following equations:

$$F_{x,out} [\text{mol h}^{-1}] = \frac{C_{x,out} F_{N_2,in}}{C_{N_2,out}} \quad (1)$$

$$r_x [\text{g h}^{-1} \text{g}_{\text{Cu}}^{-1}] = \frac{F_{x,out}}{m_{\text{Cu}}} \times MW_x \quad (2)$$

$$X_{\text{CO}_2} = \frac{\sum_{i=1}^n F_{x,out}}{F_{\text{CO}_2,in}} \quad (3)$$

$$S_{\text{MeOH}} = \frac{F_{\text{MeOH},out}}{\sum_{i=1}^n F_{x,out}} \quad (4)$$

where $F_{x,out}$ is the outlet flow rate of methanol or CO [mol h⁻¹]; $C_{x,out}$ is the outlet gas fraction of species x ; $F_{x,in}$ is the inlet flow rate of species x [mol h⁻¹]; r_x is the formation rate of methanol or CO [g h⁻¹ g_{Cu}⁻¹]; m_{Cu} is the mass of Cu used in the reaction [g]; MW_x is the molecular weight of methanol or CO [g mol⁻¹]; X_{CO_2} is the conversion of CO₂; S_{MeOH} is the selectivity to methanol. Intrinsic formation rates and selectivities were extrapolated using a second-order polynomial fit of the experimental data. At least three experimental data points were averaged for each presented data point.

Computational Details

The periodic density functional theory (DFT) calculations were carried out with the Vienna Ab Initio Simulation Package (VASP) code^{62–64}. Projector-augmented-wave (PAW) pseudopotentials were used to describe the interactions between valence electrons and ion cores, while a discrete plane wave (PW) basis set with a cutoff of 500 eV was used to treat

valence electrons⁶⁵. All geometries, adsorption energies, vibrational frequencies and Bader charges were calculated via the Generalized Gradient Approximation (GGA) including dispersion corrections by means of the BEEF-vdW density functional⁵². A 3×3 unit cell was used to construct a Mo₂C (001) surface slab using two Mo layers, with one at the top and one at the bottom of the slab, and one middle carbon layer. The Cu (111) surface model comprising a periodic 3×3 seven-layer slab and a Cu₂O (111) surface comprising a periodic 3×3 five-layer slab were constructed. 15 Å of vacuum was added in the direction perpendicular to the surface for all the models. Dipole correction was considered in all the calculations in order to correct the errors introduced by the periodic boundary conditions. Self-Consistent Field (SCF) calculations of the electronic structure were considered converged when the electronic energy change between two steps was below 10^{-5} eV. All minima geometries were optimized using an energy-based conjugate gradient algorithm until the forces acting on each atom were converged below 0.01 eV/Å. The energy of isolated molecules was determined by a single-point calculation placing each species in a box with dimensions 15 Å \times 15 Å \times 15 Å. The Nudge Elastic Band (NEB) method⁶⁶ with 8 intermediate images was used to locate transition states (TS). The transition-state structures were further refined using a Newton-based algorithm using the same convergence criteria as for the minima. All reported energy values in the text correspond to electronic energies. In all the profiles, the values have been calculated with respect to the energy of the initial reactants (in kJ mol⁻¹).

DATA AVAILABILITY All data is available from the authors upon reasonable request. Calculated DFT structures and energies are freely available at <https://doi.org/10.19061/iochem-bd-6-100>⁶⁷.

Acknowledgments

We acknowledge funding from the European Union's Horizon 2020 research and innovation program (grant agreement 800419, H.Z.), ETH Zürich (grant agreement ETH-40 17-2, Z.C.), Spanish "Ministerio de Innovación y Universidades" (grant agreement PRE2019-089647, A.V.L.), InnoSuisse - SCCER Heat and Electricity Storage (grant agreement KTI 1155002545, E.L.), ETH Zürich (grant agreement ETH-44 16-2, A.T.), European Research Council (ERC, grant agreement 819573, E.L.), ETH Postdoctoral Fellowship Program and the Marie Curie Actions for People COFUND (grant agreement 18-1 FEL 51, D.M.), Spanish MEC and the European Social Fund (grant agreement RyC-2016-19930, A.C.-V.) and Spanish "Ministerio de Innovación y Universidades" (grant agreement PGC2018-100818-A-I00, A.C.-V.). The funders had no role in study design, data collection and analysis, decision to publish or preparation of the manuscript. The authors thank ScopeM (ETH Zürich) for the use of their electron microscopy facilities and the Laboratory of Surface Science and Technology (LSST, ETH Zürich) for the use of their XPS facilities. We also acknowledge PSI Super-XAS for beamtime and thank Dr. Olga Safonova for assistance.

Author contributions

A.F. conceived the research project. H.Z. planned the experimental work. Z.C, H.Z., and D.A.K. prepared MXene-based supports. H.Z. and E.L. prepared the Cu grafted materials. H.Z. prepared, characterized and tested the catalysts, and analyzed the data. E.L. and D.M. performed solid-state NMR experiments. A.T. and E.W. performed XPS and HR-TEM imaging, respectively. A.K. and F.D. performed ICP analysis. Z.C. and P.M.A. performed XAS experiments. P.M.A. supervised XAS experiments. A.V.L., E.D.L. and A.C.-V. designed and performed DFT calculations. A.C.-V. supervised DFT calculations. C.C., A.F. and C.R.M. coordinated the research. The data were discussed among all co-authors. H.Z. and A.F. wrote the paper with contributions from all authors.

Competing interests

The authors declare no competing interests.

Figure Legends/Captions

Fig. 1. Synthesis, characterization, and activity of Cu/Mo₂CT_x/SiO₂. **a**, Schematic of the synthesis of Cu/Mo₂CT_x/SiO₂₋₅₀₀ with highly dispersed Cu sites in interaction with partially reduced Mo₂CT_x nanosheets. **b**, IR spectra of Mo₂CT_x/SiO₂₋₅₀₀ before (black) and after grafting of CuMes (red), and after treatment in H₂ at 500 °C for 2 h (blue). **c**, HAADF-EDX of Cu/Mo₂CT_x/SiO_{2-2h} (scale bar is 50 nm). **d-f**, High-resolution HAADF-STEM of Cu/Mo₂CT_x/SiO_{2-2h} recorded without exposure of the specimen to air (arrows in **d** indicate Mo vacancies in Mo₂CT_x; circles in **e** point at few-atoms-small clusters and single Cu atoms; arrows in **f** indicate the edges of Mo₂CT_x nanosheets decorated with Cu atoms). **g**, Comparison of intrinsic formation rates of CH₃OH and CO of the catalysts tested (230 °C, 25 bar, H₂/CO₂/N₂ = 3/1/1) obtained by extrapolation to zero conversion (zero contact time, see Supplementary Figures 6 and 12) together with the selectivities for CH₃OH and CO, specified above the respective bars. The Cu-ZnO-Al₂O_{3-com} denotes the commercial Cu-ZnO-Al₂O₃ catalyst (pre-treated in H₂ at 250 °C for 3.5 h before the catalytic test). **h**, Dependence of CH₃OH selectivity on CO₂ conversion by varying the contact time (see Supplementary Figure 6). **i**, Formation rates of CH₃OH and CO with a contact time of 0.06 s g mL⁻¹ on Cu/Mo₂CT_x/SiO₂ pretreated in H₂ for varying reduction times (2–12 h) at 500 °C. The dashed lines correspond to the catalyst pretreated in H₂ for 2 h followed by treatment in N₂ for an additional 2 h at 500 °C.

Fig. 2. Characterization and DFT models of the catalysts. **a**, Cu L₃VV Auger spectra (see Supplementary Table 5 for details). **b**, Temperature-programmed reduction under 5% H₂/Ar after oxidation of the specimen by 5% O₂/He at room temperature. **c**, H₂ temperature-programmed hydrogen desorption after saturation in 5% H₂/Ar. **d**, DRIFTS spectra after

desorption of CO at different temperatures (see Supplementary Figure 34 for the spectra in Kubelka-Munk units). **e–g**, Optimized structures for the H adsorption on Cu/2D-Mo₂C (**e**), Cu₄/2D-Mo₂C (**f**), and Cu/2D-Mo₂C-0.67 O ML (**g**), respectively. **h–i**, Optimized structures for the CO adsorbed on Models 4 (**h**) and 5 (**i**) with respective C–O bond distances and CO adsorption energies (E_{ads}). The interpolated oxidation states are shown for the Cu atoms (Supplementary Figure 39).

Fig. 3. Characterization and evolution of reactive intermediates. **a**, Evolution of the DRIFTS spectra over Cu/Mo₂CT_x/SiO_{2-2h} (230 °C, 25 bar, H₂/CO₂/N₂ = 3/1/1) with TOS. **b**, Operando DRIFTS GC data of CO₂ hydrogenation over Cu/SiO_{2-2h} and Cu/Mo₂CT_x/SiO_{2-2h} and corresponding evolution of the reaction rate. Peaks at 2857 and 2959 cm⁻¹ were used to assess the intensity of formate and methoxy species, respectively. **c**, Solid-state cross-polarization magic angle spinning (CP-MAS) ¹³C NMR spectra of Cu/Mo₂CT_x/SiO_{2-2h} and Mo₂CT_x/SiO_{2-2h} after exposure of H₂/¹³CO₂ (ca. 3/1) for 12 h at 230 °C and 5 bar.

Fig. 4. DFT-computed energy profiles. Considered reactions are CO₂ and 2H₂, or CO₂ and 1H₂, to form methanol and O* (blue trace), or CO and H₂O (magenta trace, RWGS reaction), respectively. Energies are shown with respect to the initial reactants in kJ mol⁻¹ (E_{rel}). Only selected intermediates and transition states (TS) are presented with their respective energies shown in parenthesis. See Supplementary Figure 44 for the structures of other intermediates and transition states and for their energies.

References

1. Goeppert, A., Czaun, M., Jones, J.-P., Surya Prakash, G. K. & Olah, G. A. Recycling of carbon dioxide to methanol and derived products – closing the loop. *Chem. Soc. Rev.* **43**, 7995–8048 (2014).
2. Olah, G. A. Beyond Oil and Gas: The Methanol Economy. *Angew. Chem. Int. Ed.* **44**, 2636–2639 (2005).

3. Behrens, M. *et al.* The Active Site of Methanol Synthesis over Cu/ZnO/Al₂O₃ Industrial Catalysts. *Science* **336**, 893–897 (2012).
4. Lunkenbein, T., Schumann, J., Behrens, M., Schlögl, R. & Willinger, M. G. Formation of a ZnO Overlayer in Industrial Cu/ZnO/Al₂O₃ Catalysts Induced by Strong Metal–Support Interactions. *Angew. Chem. Int. Ed.* **54**, 4544–4548 (2015).
5. Lee, J. S., Lee, K. H., Lee, S. Y. & Kim, Y. G. A comparative study of methanol synthesis from CO₂/H₂ and CO/H₂ over a Cu/ZnO/Al₂O₃ catalyst. *J. Catal.* **144**, 414–424 (1993).
6. Kattel, S., Ramírez, P. J., Chen, J. G., Rodriguez, J. A. & Liu, P. Active sites for CO₂ hydrogenation to methanol on Cu/ZnO catalysts. *Science* **355**, 1296–1299 (2017).
7. Martin, O. & Pérez-Ramírez, J. New and revisited insights into the promotion of methanol synthesis catalysts by CO₂. *Catal. Sci. Technol.* **3**, 3343–3352 (2013).
8. Rozovskii, A. Y. & Lin, G. I. Fundamentals of methanol synthesis and decomposition. *Top. Catal.* **22**, 137–150 (2003).
9. Zhang, Y., Sun, Q., Deng, J., Wu, D. & Chen, S. A high activity Cu/ZnO/Al₂O₃ catalyst for methanol synthesis: Preparation and catalytic properties. *Appl. Catal. Gen.* **158**, 105–120 (1997).
10. Klier, K., Chatikavanij, V., Herman, R. G. & Simmons, G. W. Catalytic synthesis of methanol from CO/H₂: IV. The effects of carbon dioxide. *J. Catal.* **74**, 343–360 (1982).
11. Ruland, H. *et al.* CO₂ Hydrogenation with Cu/ZnO/Al₂O₃: A Benchmark Study. *ChemCatChem* **12**, 3216–3222 (2020).
12. Lam, E. *et al.* Isolated Zr Surface Sites on Silica Promote Hydrogenation of CO₂ to CH₃OH in Supported Cu Catalysts. *J. Am. Chem. Soc.* **140**, 10530–10535 (2018).
13. Larmier, K. *et al.* CO₂-to-Methanol Hydrogenation on Zirconia-Supported Copper Nanoparticles: Reaction Intermediates and the Role of the Metal–Support Interface. *Angew. Chem. Int. Ed.* **56**, 2318–2323 (2017).
14. Kattel, S., Yan, B., Yang, Y., Chen, J. G. & Liu, P. Optimizing Binding Energies of Key Intermediates for CO₂ Hydrogenation to Methanol over Oxide-Supported Copper. *J. Am. Chem. Soc.* **138**, 12440–12450 (2016).
15. Noh, G. *et al.* Selective Hydrogenation of CO₂ to CH₃OH on Supported Cu Nanoparticles Promoted by Isolated Ti^{IV} Surface Sites on SiO₂. *ChemSusChem* **12**, 968–972 (2019).
16. Graciani, J. *et al.* Highly active copper-ceria and copper-ceria-titania catalysts for methanol synthesis from CO₂. *Science* **345**, 546–550 (2014).

17. Lam, E. *et al.* CO₂ Hydrogenation on Cu/Al₂O₃: Role of the Metal/Support Interface in Driving Activity and Selectivity of a Bifunctional Catalyst. *Angew. Chem. Int. Ed.* **58**, 13989–13996 (2019).
18. Studt, F. *et al.* The Mechanism of CO and CO₂ Hydrogenation to Methanol over Cu-Based Catalysts. *ChemCatChem* **7**, 1105–1111 (2015).
19. Docherty, S. R. & Copéret, C. Deciphering Metal–Oxide and Metal–Metal Interplay via Surface Organometallic Chemistry: A Case Study with CO₂ Hydrogenation to Methanol. *J. Am. Chem. Soc.* **143**, 6767–6780 (2021).
20. Yao, S. *et al.* Atomic-layered Au clusters on α -MoC as catalysts for the low-temperature water-gas shift reaction. *Science* **357**, 389–393 (2017).
21. Lin, L. *et al.* Low-temperature hydrogen production from water and methanol using Pt/ α -MoC catalysts. *Nature* **544**, 80–83 (2017).
22. Dong, J., Fu, Q., Jiang, Z., Mei, B. & Bao, X. Carbide-Supported Au Catalysts for Water–Gas Shift Reactions: A New Territory for the Strong Metal–Support Interaction Effect. *J. Am. Chem. Soc.* **140**, 13808–13816 (2018).
23. Zhang, X. *et al.* Highly Dispersed Copper over β -Mo₂C as an Efficient and Stable Catalyst for the Reverse Water Gas Shift (RWGS) Reaction. *ACS Catal.* **7**, 912–918 (2017).
24. Posada-Pérez, S. *et al.* The conversion of CO₂ to methanol on orthorhombic β -Mo₂C and Cu/ β -Mo₂C catalysts: mechanism for admetal induced change in the selectivity and activity. *Catal. Sci. Technol.* **6**, 6766–6777 (2016).
25. Anasori, B., Lukatskaya, M. R. & Gogotsi, Y. 2D metal carbides and nitrides (MXenes) for energy storage. *Nat. Rev. Mater.* **2**, 16098 (2017).
26. Sarycheva, A. *et al.* 2D titanium carbide (MXene) for wireless communication. *Sci. Adv.* **4**, eaau0920 (2018).
27. Naguib, M. *et al.* Two-Dimensional Nanocrystals Produced by Exfoliation of Ti₃AlC₂. *Adv. Mater.* **23**, 4248–4253 (2011).
28. Deeva, E. B. *et al.* In Situ XANES/XRD Study of the Structural Stability of Two-Dimensional Molybdenum Carbide Mo₂CT_x Implications for the Catalytic Activity in the Water–Gas Shift Reaction. *Chem. Mater.* **31**, 4505–4513 (2019).
29. Diao, J. *et al.* Ti₃C₂T_x MXene Catalyzed Ethylbenzene Dehydrogenation: Active Sites and Mechanism Exploration from both Experimental and Theoretical Aspects. *ACS Catal.* **8**, 10051–10057 (2018).

30. Kurlov, A. *et al.* Exploiting two-dimensional morphology of molybdenum oxycarbide to enable efficient catalytic dry reforming of methane. *Nat. Commun.* **11**, 4920 (2020).
31. Li, Z. *et al.* Reactive metal–support interactions at moderate temperature in two-dimensional niobium-carbide-supported platinum catalysts. *Nat. Catal.* **1**, 349–355 (2018).
32. Li, Z. *et al.* Two-dimensional transition metal carbides as supports for tuning the chemistry of catalytic nanoparticles. *Nat. Commun.* **9**, 5258 (2018).
33. Lang, Z. *et al.* MXene Surface Terminations Enable Strong Metal–Support Interactions for Efficient Methanol Oxidation on Palladium. *ACS Appl. Mater. Interfaces* **12**, 2400–2406 (2020).
34. Zhao, D. *et al.* MXene (Ti₃C₂) Vacancy-Confined Single-Atom Catalyst for Efficient Functionalization of CO₂. *J. Am. Chem. Soc.* **141**, 4086–4093 (2019).
35. Morales-García, Á., Fernández-Fernández, A., Viñes, F. & Illas, F. CO₂ abatement using two-dimensional MXene carbides. *J. Mater. Chem. A* **6**, 3381–3385 (2018).
36. Copéret, C. *et al.* Surface Organometallic and Coordination Chemistry toward Single-Site Heterogeneous Catalysts: Strategies, Methods, Structures, and Activities. *Chem. Rev.* **116**, 323–421 (2016).
37. Fedorov, A., Liu, H.-J., Lo, H.-K. & Copéret, C. Silica-Supported Cu Nanoparticle Catalysts for Alkyne Semihydrogenation: Effect of Ligands on Rates and Selectivity. *J. Am. Chem. Soc.* **138**, 16502–16507 (2016).
38. Zhang, J. *et al.* Single platinum atoms immobilized on an MXene as an efficient catalyst for the hydrogen evolution reaction. *Nat. Catal.* **1**, 985 (2018).
39. Lauritsen, J. V. *et al.* Location and coordination of promoter atoms in Co- and Ni-promoted MoS₂-based hydrotreating catalysts. *J. Catal.* **249**, 220–233 (2007).
40. Zhu, G. *et al.* Enhanced CO₂ electroreduction on armchair graphene nanoribbons edge-decorated with copper. *Nano Res.* **10**, 1641–1650 (2017).
41. Ro, I. *et al.* Role of the Cu-ZrO₂ Interfacial Sites for Conversion of Ethanol to Ethyl Acetate and Synthesis of Methanol from CO₂ and H₂. *ACS Catal.* **6**, 7040–7050 (2016).
42. Halim, J. *et al.* Synthesis and Characterization of 2D Molybdenum Carbide (MXene). *Adv. Funct. Mater.* **26**, 3118–3127 (2016).
43. Cramer, S. P., Eccles, T. K., Kutzler, F. W., Hodgson, K. O. & Mortenson, L. E. Molybdenum x-ray absorption edge spectra. The chemical state of molybdenum in nitrogenase. *J. Am. Chem. Soc.* **98**, 1287–1288 (1976).

44. Chen, A. *et al.* Structure of the catalytically active copper–ceria interfacial perimeter. *Nat. Catal.* **2**, 334–341 (2019).
45. Newton, M. A. *et al.* Unwanted effects of X-rays in surface grafted copper(II) organometallics and copper exchanged zeolites, how they manifest, and what can be done about them. *Phys. Chem. Chem. Phys.* **22**, 6826–6837 (2020).
46. Frenkel, A. I. Solving the structure of nanoparticles by multiple-scattering EXAFS analysis. *J. Synchrotron Radiat.* **6**, 293–295 (1999).
47. de Jong, K. P., Geus, J. W. & Joziassse, J. An infrared spectroscopic study of the adsorption of carbon monoxide on silica-supported copper particles. *Appl. Surf. Sci.* **6**, 273–287 (1980).
48. Smith, M. L., Kumar, N. & Spivey, J. J. CO Adsorption Behavior of Cu/SiO₂, Co/SiO₂, and CuCo/SiO₂ Catalysts Studied by in Situ DRIFTS. *J. Phys. Chem. C* **116**, 7931–7939 (2012).
49. Subramanian, N. D. *et al.* A DRIFTS study of CO adsorption and hydrogenation on Cu-based core–shell nanoparticles. *Catal. Sci. Technol.* **2**, 621 (2012).
50. Cox, D. F. & Schulz, K. H. Interaction of CO with Cu⁺ cations: CO adsorption on Cu₂O (100). *Surf. Sci.* **249**, 138–148 (1991).
51. Fisher, I. A. & Bell, A. T. In situ infrared study of methanol synthesis from H₂/CO over Cu/SiO₂ and Cu/ZrO₂/SiO₂. *J. Catal.* **178**, 153–173 (1998).
52. Wellendorff, J. *et al.* Density functionals for surface science: Exchange–correlation model development with Bayesian error estimation. *Phys. Rev. B* **85**, 235149 (2012).
53. Baiker, A., Kilo, M., Maciejewski, M., Menzi, S. & Wokaun, A. Hydrogenation of CO₂ Over Copper, Silver and Gold/Zirconia Catalysts: Comparative Study of Catalyst Properties and Reaction Pathways. in *Studies in Surface Science and Catalysis* (eds. Guenzi, L., Solymosi, F. & Tétényi, P.) vol. 75 1257–1272 (Elsevier, 1993).
54. Fehr, S. M. & Krossing, I. Spectroscopic Signatures of Pressurized Carbon Dioxide in Diffuse Reflectance Infrared Spectroscopy of Heterogeneous Catalysts. *ChemCatChem* **12**, 2622–2629 (2020).
55. Quan, J. *et al.* Vibration-driven reaction of CO₂ on Cu surfaces via Eley–Rideal-type mechanism. *Nat. Chem.* **11**, 722–729 (2019).
56. Baxter, R. J. & Hu, P. Insight into why the Langmuir–Hinshelwood mechanism is generally preferred. *J. Chem. Phys.* **116**, 4379–4381 (2002).

57. Cossu, G., Rossi, A., Arcifa, A. & Spencer, N. D. Development and application of a cost-effective transfer cell for X-ray photoelectron spectroscopy. in *Incontro di Spettroscopia Analitica ISA* (2018).
58. Clark, A. H., Imbao, J., Frahm, R. & Nachtegaal, M. ProQEXAFS: a highly optimized parallelized rapid processing software for QEXAFS data. *J. Synchrotron Radiat.* **27**, 551–557 (2020).
59. Ravel, B. & Newville, M. ATHENA, ARTEMIS, HEPHAESTUS: data analysis for X-ray absorption spectroscopy using IFEFFIT. *J. Synchrotron Radiat.* **12**, 537–541 (2005).
60. Fung, B. M., Khitrin, A. K. & Ermolaev, K. An Improved Broadband Decoupling Sequence for Liquid Crystals and Solids. *J. Magn. Reson.* **142**, 97–101 (2000).
61. Tsoukalou, A. *et al.* Structural Evolution and Dynamics of an In₂O₃ Catalyst for CO₂ Hydrogenation to Methanol: An Operando XAS-XRD and In Situ TEM Study. *J. Am. Chem. Soc.* **141**, 13497–13505 (2019).
62. Kresse, G. & Hafner, J. Ab initio molecular dynamics for liquid metals. *Phys. Rev. B* **47**, 558–561 (1993).
63. Kresse, G. & Hafner, J. Ab initio molecular-dynamics simulation of the liquid-metal--amorphous-semiconductor transition in germanium. *Phys. Rev. B* **49**, 14251–14269 (1994).
64. Kresse, G. & Furthmüller, J. Efficiency of ab-initio total energy calculations for metals and semiconductors using a plane-wave basis set. *Comput. Mater. Sci.* **6**, 15–50 (1996).
65. Blöchl, P. E. Projector augmented-wave method. *Phys. Rev. B* **50**, 17953–17979 (1994).
66. Jonsson, H., Mills, G. & Jacobsen, K. Nudged elastic band method for finding minimum energy paths of transitions. in *Classical and Quantum Dynamics in Condensed Phase Simulations* 385–404 (1998).
doi:10.1142/9789812839664_0016.
67. Álvarez-Moreno, M., de Graaf, C., Lopez, N., Maseras, F., Poblet, J. M. & Bo, C. *J. Chem. Inf. Model.* **55**, 95–103 (2015).